Computational and experimental characterization of high-brightness beams for femtosecond electron imaging and spectroscopy

J. Portman, H. Zhang, Z. Tao, K. Makino, M. Berz, P. M. Duxbury, and C.-Y. Ruan
Physics and Astronomy Department, Michigan State University, East Lansing, Michigan 48824, USA

(Received 12 August 2013; accepted 8 December 2013; published online 20 December 2013)

Using a multilevel fast multipole method, coupled with the shadow imaging of femtosecond photoelectron pulses for validation, we quantitatively elucidate the photocathode, space charge, and virtual cathode physics, which fundamentally limit the spatiotemporal and spectroscopic resolution and throughput of ultrafast electron microscope (UEM) systems. We present a simple microscopic description to capture the nonlinear beam dynamics based on a two-fluid picture and elucidate an unexpected dominant role of image potential pinning in accelerating the emittance growth process. These calculations set theoretical limits on the performance of UEM systems and provide useful guides for photocathode design for high-brightness electron beam systems. [http://dx.doi.org/10.1063/1.4855435]

High-resolution transmission electron microscopy (TEM) using coherent electron beams from field emission guns (FEGs), along with aberration correction, has enabled the atomic resolution imaging of complex materials.[1] More recently, advances in developing femtosecond (fs) photoemitters and retrofitting them into diffraction and microscopy systems has further opened up the prospects of multi-functional probing at the fs-nm scale[2–6] with ultrafast structural and spectroscopic resolution at the single particle or domain level.[7] Nonetheless realization of the desired space-time resolution with sufficient sensitivity is severely challenged[5] by the so-called space charge effects,[2,8–11] which come primarily in two forms. The first is the collective space charge effect, manifested in electron pulse lengthening from the development of momentum-space correlation (chirping), which is significantly accelerated by the internal Coulombic fields of the electron pulse.[8] This issue is nonetheless remediable by modern accelerator technology for reversing the momentum distribution resulting in longitudinal refocusing, rather similar to static electron optical lenses handling the transverse phase space. This concept of a temporal lens based on one or more radio frequency (RF) cavity "bunchers" has recently been demonstrated in a 100 keV electron beam system.[12] The second form of the space charge effect, which is the primary concern here, is stochastic in origin and fundamentally limits the space, time, and spectroscopic resolution achievable in an ultrafast electron microscope (UEM). This effect, termed stochastic space charge effect, is correlated with an irreversible growth in beam emittance, or the phase space volume, due to fluctuating components of the nonlinear electron dynamics. Such emittance growth has been observed in TEM, predominately at strong beam crossovers,[13] resulting in spectroscopic and image blurring. In the short pulse UEM regime, it is strongly coupled to virtual cathode (VC) formation that occurs during fs intense photoelectron pulse generation. The stochastic space charge and virtual cathode effects and their remediation are core issues to be addressed for the development of the next generation of high-brightness UEMs with active optical components to correct the phase space.[12,14–17]

In this Letter, we employ the state-of-the-art multilevel fast multiple method (MLFMM) within the framework of differential algebra[18] of COSY INFINITY for a first quantitative effort at tackling the stochastic space charge effect, at a numerical efficiency of nearly O(N).[19] We address open questions regarding the emittance growth near the virtual cathode threshold[20] in a DC acceleration field and the influence of the dynamical image charge potential on the fs electron pulse activation, for establishing high-brightness beams. The simulation is directly compared with ultrafast shadow imaging experiments designed to characterize the photoelectron dynamics in the same regime, in order to validate the ability of the MLFMM approach to faithfully reproduce nonlinear beam dynamics without resorting to fitting parameters.[8,11] We provide a microscopic description of the virtual cathode formation as driven by instabilities and image potential that promote a dramatic emittance growth and current limitation. We show that the transient phase space structure of the electron bunches is well described as a two-fluid system with a dominant ellipsoidal component undergoing laminar flow under moderately high acceleration fields, while a smaller turbulent component is determined by the initial phase space structure. This unique two-fluid characteristic subtly controlled by the source geometry and initial conditions provides a handle for controlling the emittance growth at high-intensity beam generation without significantly sacrificing the spatial and temporal-spectroscopic resolutions.

As a grid-free approach, MLFMM treats the local interaction in a natural way without artificial smoothing, allowing crucial handling of the nonlinear dynamics near the photocathode where the electron beam is at low energy and high density. During this period, the electron density distributions are most sensitive to the initial phase space, which are probed directly using the ultrafast shadow imaging techniques as shown in Fig. 1, providing the crucial validation for MLFMM (see Ref. 11 for experimental details). In Fig. 1(a), the longitudinal density profiles (circles at 50 and 80 ps) extracted from the shadow images evidence the accelerated expansion driven by space-charge fields at $N_e = 1 \times 10^8$, and are compared with the MLFMM simulations reproduced under the same conditions. In the simulation, we use the three-step model[21] for creating the photoelectrons, in which we set the Fermi energy 5 eV, and work function 4.45 eV to

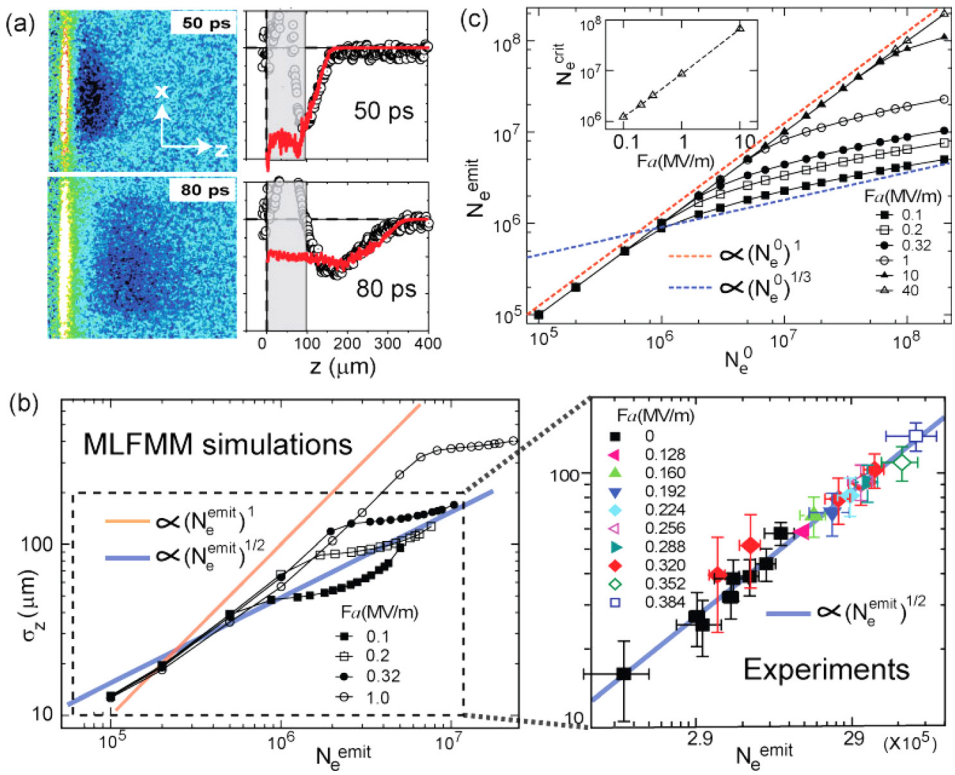

FIG. 1. (a) Comparisons of MLFMM simulations of longitudinal charge density profiles (red lines) and data (circles) extracted from the shadow imaging experiments at 50 and 80 ps. (b) Sublinear scaling of longitudinal bunch size σ_z versus number of electrons emitted (N_e^{emit}) taken at 120 ps from MLFMM simulations (left panel), and compared to the shadow imaging data (right panel). (c) N_e^{emit} versus the number of generated electrons (N_e^0) for various extraction fields (F_a), showing evidence of virtual cathode formation. Inset: Threshold number of electrons (N_e^{crit}) for virtual cathode formation as a function of F_a.

model the gold photocathode, and photon energy 4.66 eV. The laser pulses are Gaussian spatially and temporally with standard deviations: $\sigma_r^l = 91\,\mu$m and $\sigma_t^l = 21$ fs, respectively, according to the experiments. A fine time step of $0.06\sigma_t$ is used for the initial period of $6\sigma_t^l$ during photoemission, whereas, in the following 120 ps of the beam dynamics, the step size is progressively increased up to 0.5 ps. Macroparticles are used in simulating $N_e > 10^6$ after checking with the corresponding N-particle simulations for consistency. The dynamics equations are solved by the fourth order Runge-Kutta integrator.[19]

The agreement between the simulation and experiment is excellent for the leading portion of the beams. In the trailing portion close to the cathode (Fig. 1(a), shaded regions), the charge density is not fully accessible experimentally due to strong surface scattering of the probe beam.[11] MLFMM shows that near the surface the charge density deviates from Gaussian, reflecting the formation of VC. Previously, to understand the space-charge-led expansion, shadow imaging experiments indicated an unusual universality in sub-linear scaling of bunch longitudinal size σ_z versus N_e (more specifically, a power-law with exponent $\alpha \sim 0.5$) over a wide range of laser fluences (F) and extraction fields (F_a).[11] MLFMM is used here to reproduce this trend under relevant conditions (boxed region) depicted in Fig. 1(b) (left panel), compared with the experiments (right panel). The close resemblance between the two are non-trivial, albeit careful examination shows this universality is partly coincidental as only when the bunch is in the sub-VC regime does a truly universal behavior, with α between 0.5 and 1, occur; however, above the VC threshold the increase of σ_z is reduced and the overall trend is consistent with $\alpha = 0.5$ (solid blue lines) for $F_a < 1$ MV/m. We note that the emitted particle number, hereafter labeled as N_e^{emit}, is determined at t = 120 ps, which, due to VC effect, is generally smaller than the initial population N_e^0, which in MLFMM is proportional to the applied laser fluence.

The analytical model[20] of VC effect in the short-pulse limit showed that a higher current density may be drawn than anticipated by the Child-Langmuir limiting current, which gives an unrealistic linear dependence of such limit over pulse width. The MLFMM allows microscopic simulations of the processes driven by nonlinear beam dynamics. First, we compare N_e^{emit} and N_e^0 as shown in Fig. 1(c). The VC limits can be identified by the deviations from the linear correlation (dashed black line) to the ones above the threshold under all extraction fields ($F_a = 0.1$–40 MV/m). The VC formation, N_e^{crit}, while found to be linear as a function of F_a [inset of Fig. 1(c)], leads to a non-vanishing power-law exponent ~1/3 (dashed blue line) for the current increase.

The microscopic dynamics attributing to VC formation for emittance growth are rather complex as demonstrated in the 2D color maps of the charge distribution projected along the x and z axes in the rest frame of the bunches, shown in Fig. 2. The charge flows are depicted by the arrows overlaid on the images. We find that at the embryonic stage ($t = 0.63$ ps) the beam is generically more turbulent as memory of the initial electronic thermal emittance still dominates the motion of the electrons, as shown in Fig. 2(a). The initial charge distribution is near Gaussian, derived from the driving laser field. Propelled by the strong self-fields of the space charges, the bunch rapidly expands, whereas the fields associated with the image charges on surface may present an external focusing channel. In our cases the fs photo-emitted electrons are initially in a pancake geometry ($\sigma_z \sim 10$ nm, $\sigma_x \sim 100\,\mu$m), and the dynamical rearrangements of the space charges tend to make the self-fields more linear, consequently more laminar beams will form eventually, as shown

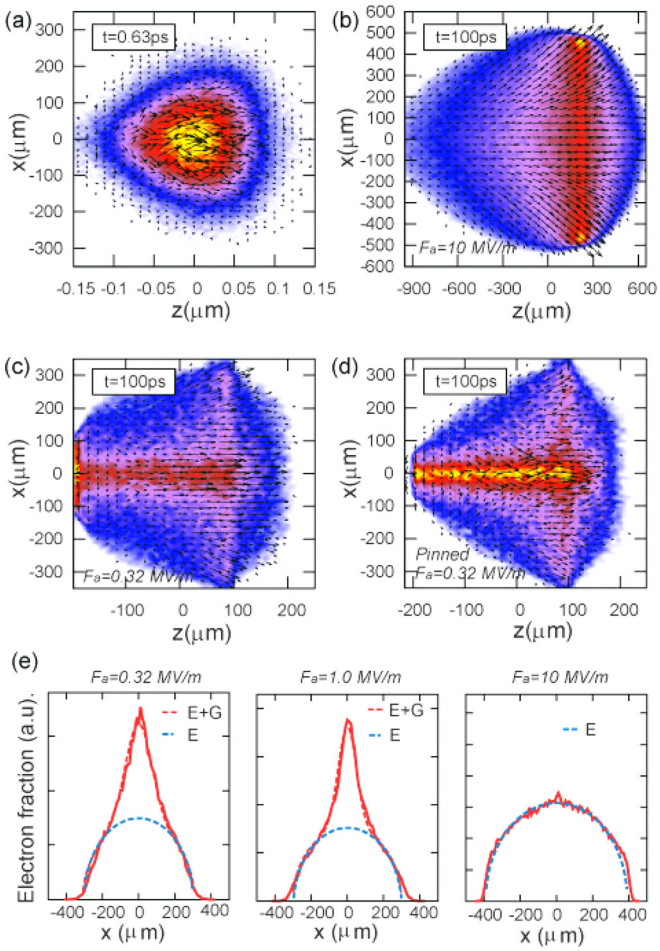

FIG. 2. (a)–(d) 2D color map of charge density projected to the x-z plane in the center-of-mass frame. The arrows represent local electron velocity. Panel (a) shows the generic map at the embryonic stage, whereas panels (b)–(d) show the maps taken at 100 ps for different extraction field ($F_a = 10$ and 0.32 MV/m), and in panel (d) the image charges are pinned on the surface. (e) Transverse charge density profiles under different extraction fields F_a (0.32, 1, and 10 MV/m), fitted by a combination of Gaussian (G) and ellipsoidal (E) functions. Note that the number of emitted electrons (2×10^7) is the same in all three cases.

in Figs. 2(b)–2(d) calculated at 100 ps. The intricate effects derived from the surface fields, which have a strength of 10 MV/m based on $F_s = N_e^{emit}/(\pi 2ln(2)\sigma_x^2)$ and $N_e^{emit} = 2 \times 10^7$ in all three cases, are clearly seen in the presence of the turbulent flows, when $F_s > F_a$. In the $F_a = 10$ MV/m case [Fig. 2(b)], the beam becomes fully laminar. In contrast, at $F_a = 0.32$ MV/m [Figs. 2(c) and 2(d)], non-laminar flows are present, especially when image charges are pinned on the surface as shown in Fig. 2(d).

The turbulent flow induced in forming a high-density beam is relevant to the Boersch effect,[13] which manifests stochastic processes causing uncorrectable defocusing of the beams. This effect differs from the blurring induced by the linear portion of space-charge fields[15] and may be suppressed by generating uniformly filled ellipsoidal beams, which were recently demonstrated[22] by creating pancake bunches that evolve in the presence of a high-gradient RF photogun.[23] Such a uniform 3D elliptical electron bunch has linear self-fields, and will evolve as an ellipse in all directions under any linear transport environment, even though its dimensionality ratio will change. Therefore, the image blurring caused by the self-field-driven beam expansion can be fully corrected by deploying appropriate beam transport optics, including compression[12,14] and aberration corrections,[1] to achieve the desired resolution at the target.[11] Reducing the Boersch effect at beam generation is, therefore, critical for enhancing performance of high-brightness UEM designs.

We analyze the nature of the coexisting two fluids (turbulent and laminar) observed in the space-charge-dominated beams. The transverse charge density profiles of the beams generated at $F_a = 0.32$, 1, and 10 MV/m are extracted, and fitted with a linear combination of Gaussian (G) and uniform-filled ellipsoidal (E) functions, as depicted in Fig. 2(e). At $F_a = 10$ MV/m, the laminar beam is perfectly described by the ellipsoidal function, signifying the formation of the 2D ellipse at this stage. In contrast, at $F_a = 0.32$ and 1 MV/m, the flow is not fully laminar, and the nonlaminar portion can be well described by a Gaussian with extended tails representative of the Maxwellian-like (thermal) population, which coexists with the 2D ellipse as evidenced by the fits. The predominance of the 2D ellipse, which accounts for more than 65% of the electrons even under the lowest F_a, is somewhat surprising, as ellipsoidal beam formation fully driven by self-fields is expected only at the zero surface charge limit, i.e., $F_s \ll F_a$ (Refs. 22 and 23).

We further examine the scaling of the normalized rms emittance[23] versus charge filling, namely, transverse emittance $\epsilon_x(N_e^{emit})$ and longitudinal emittance $\epsilon_z(N_e^{emit})$. We consider two image charge models where the first model considers pinned surface charges and the second treats the image charges as fully responsive to the motion of the electrons, providing reasonable limiting cases for the response dynamics of the image charges. Fig. 3 depicts the emittance at 120 ps calculated for various N_e^{emit} and F_a and for the image charge pinning scenario. In $\epsilon_x(N_e^{emit})$ [Fig. 3(a)], we can clearly see a strong increase of ϵ_x after N_e^{crit} is reached in all F_a data, evidencing the VC-driven ϵ_x growth. When the image charges are pinned, ϵ_x growth is nearly doubled, but N_e^{crit} is the same (see comparison in the $F_a = 0.32$ MV/m cases). The inset of Fig. 3(a) shows the temporal evolutions of ϵ_x at $F_a = 0.32$ and 1.0 MV/m (all with 10^7 electrons), where generally ϵ_x reaches a steady state after 40 ps. The region exhibiting emittance-growth-free dynamics is well correlated with the region where the 2D elliptical pulse structure dominates. In contrast, in $\epsilon_z(N_e^{emit})$, as presented in Fig. 3(b), we see little or no VC effect at play as increases in ϵ_z seem to follow a universal trend, uninterrupted by the VC formation. This insensitivity to external field settings is an indicator that with pancake bunch generation the longitudinal emittance is primarily driven by the strong internal longitudinal fields and nonlinearities. This is particularly evident from the very similar $\epsilon_z(t)$ calculated for $N_e^{emit} = 10^7$ under three very different external field values (F_a), as shown in the inset.

The quantitative emittance scalings elucidated here provide some useful guides for the design of high-brightness UEMs. First, the beam's emittance fundamentally sets the theoretical resolution limits. The coherence length L_t is constrained by $\epsilon_x : L_t \leq \sigma_r^e \epsilon_0 / 2\epsilon_x$, where $\epsilon_0 = h/(m_0 c)$ is the emittance quantum, h is Planck's constant, and σ_r^e is the electron beam radius. The temporal (Δt) and energy (ΔE) resolutions are constrained by $\epsilon_z : \epsilon_z \leq \Delta t \Delta E/(\gamma m_0 c)$, where γ is

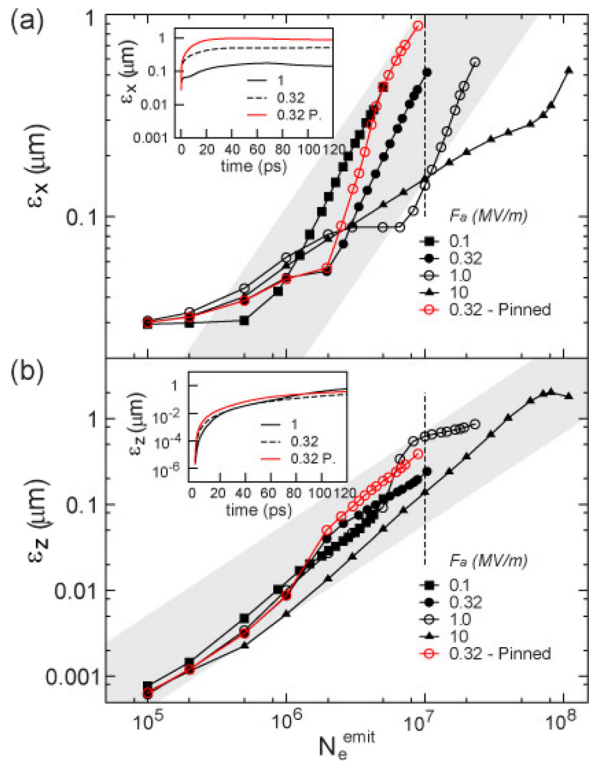

FIG. 3. (a) Transverse emittance ϵ_x dependence on number of emitted electrons (N_e^{emit}) and extraction field F_a. (b) Longitudinal emittance ϵ_z dependence on N_e^{emit} and F_a calculated at 120 ps. The insets in the panels show the time dependence of ϵ_x and ϵ_z for three selected cases at $N_e^{emit} = 10^7$. The shaded regions depict the trend for linear emittance growth.

the relativistic Lorentz factor. Lower emittance is also favored for reducing the aberrations and consequently improving the phase contrast in microscopy.[1] In considering the sensitivity of UEMs, the emittance is linked to the 6D beam brightness: $B_{6D} = N_e/(\epsilon_x^2\epsilon_z)$, or the degeneracy $\eta = B_{6D}\epsilon_0^3$ by normalizing B_{6D} to the emittance quantum.[7] The degeneracy[1,7] for different operational regimes is depicted in Fig. 4, where the theoretical limit of η is 2, limited by Pauli exclusion (considering both spins). One measure of improved performance is the increase in η by increasing N_e^{emit} until the emittance volume $\epsilon_x\epsilon_y\epsilon_z$ starts to increase rapidly due to VC effects. In conventional TEM, the lowest

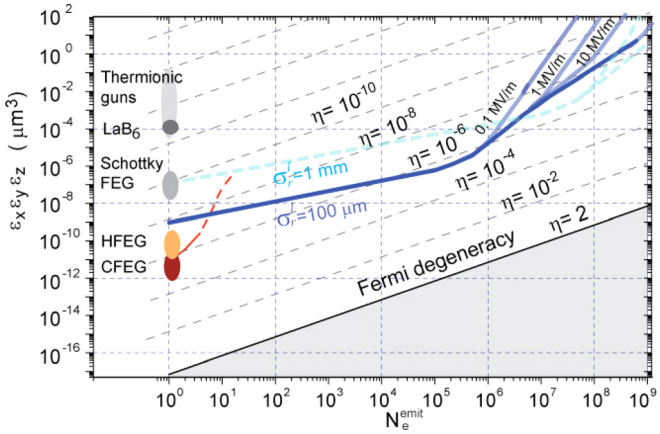

FIG. 4. The 6D emittance $\epsilon_x\epsilon_y\epsilon_z$ versus the number of emitted electrons N_e^{emit} for the extended electron sources with sizes σ_r^I (100 μm, 1 mm), thermionic guns,[1] Schottky, cold field-emission guns (CFEG), and heated field-emission guns (HFEG).[1]

emittance is established with a cold FEG having a 6D emittance volume of 10^{-11} μm^3 or $\eta \sim 10^{-5}$ [$\epsilon_x \sim 1$ nm and $\epsilon_z \sim 10$ pm (statistical)].[1] In contrast, a flat metallic photocathode widely used in ultrafast electron diffraction has a degraded $\epsilon_x \sim 20 - 200$ nm [Fig. 3(a)]. However, the extended sources driven in the pancake regime have the emittance volume $\epsilon_x\epsilon_y\epsilon_z$ scale favorably, leading to a gain in η for electron bunches up to $N_e^{emit} = 10^6$ for a typical laser pulse size. Using the highest acceleration fields, e.g., $F_a = 10$ MV/m in DC guns or $F_a \sim 100$ MV/m in RF guns,[24] does not improve η or ϵ, but instead increases N_e^{crit} without substantively compromising performance. In these high charge limits, the degeneracy figures are comparable to FEGs, implying that similar performance (with proper phase space manipulation) could be reached using a portion of the transverse emittance volume, for example by using apertures, whereas in the single-shot limit performance equivalent to those of thermionic guns is expected.

However, ϵ_z does not scale as favorably as ϵ_x leading to some reduction in time and energy resolution. Increasing N_e^{emit} always leads to an ϵ_z increase [almost linearly, see Fig. 3(b)]. To achieve combined 100 fs–1 eV resolution no more than $N_e^{emit} = 10^3$ can be deployed based on $\Delta E \geq \epsilon_z \gamma m_0 c/\Delta t$. In comparison, there is no gain in multi-electron mode using sharp emitters (FEGs or atom-sized emitters) due to their poor emittance scaling with N_e (as in the charge-pinning scenario). For example, when reducing the radius of the emitting area from 100 μm to 10 μm, the emittance is initially reduced but scales unfavorably so that there is a crossover at about 100 fs after which the 6D emittance for the smaller emitter become greater. The VC regime also sets in at a lower value of N_e^0, leading to nearly two orders of magnitude fewer emitted electrons. Beyond optimizing the cathode geometry, laser pulse shaping of initial bunches[17] from Gaussian to ellipsoidal can help reduce the emittance by nearly a factor of 2, moreover design of sources with lower initial thermal emittance and appropriate emittance compensation[16] will further improve the performance.

We acknowledge support from US National Science Foundation under Grant No. NSF-DMR 1126343 and a seed grant from the MSU Foundation for developing ultrafast electron microscope.

[1]*Science of Microscopy*, edited by P. W. Hawkes and J. C. H. Spence (Springer, New York, 2008).
[2]R. Srinivasan, V. A. Lobastov, C.-Y. Ruan, and A. H. Zewail, Helv. Chim. Acta **86**, 1761 (2003).
[3]G. Sciani and R. J. D. Miller, Rep. Prog. Phys. **74**, 096101 (2011).
[4]C.-Y. Ruan, Y. Murooka, R. K. Raman, R. A. Murdick, R. J. Worhatch, and A. Pell, Microsc. Microanal. **15**, 323 (2009).
[5]B. W. Reed, M. R. Armstrong, N. D. Browning, G. H. Campbell, J. E. Evans, T. LaGrange, and D. J. Masiel, Microsc. Microanal. **15**, 272 (2009).
[6]P. Zhu, J. Cao, Y. Zhu, J. Geck, Y. Hidaka, S. Pjerov, T. Ritschel, H. Berger, Y. Shen, R. Tobey *et al.*, Appl. Phys. Lett. **103**, 071914 (2013).
[7]A. H. Zewail and J. M. Thomas, *4D Electron Microscopy: Imaging in Space and Time* (Imperial College Press, London, 2010).
[8]B. J. Siwick, J. R. Dwyer, R. E. Jordan, and R. J. D. Miller, J. Appl. Phys. **92**, 1643 (2002).
[9]B. W. Reed, J. Appl. Phys. **100**, 034916 (2006).
[10]A. Gahlmann, S. T. Park, and A. H. Zewail, Phys. Chem. Chem. Phys. **10**, 2894 (2008).

[11]Z. Tao, H. Zhang, P. M. Duxbury, M. Berz, and C.-Y. Ruan, J. Appl. Phys. **111**, 044316 (2012).
[12]T. van Oudheusden, P. L. E. M. Pasmans, S. B. van der Geer, M. J. de Loos, M. J. van der Wiel, and O. J. Luiten, Phys. Rev. Lett. **105**, 264801 (2010).
[13]H. Boersch, Z. Phys. **139**, 115 (1954).
[14]J. B. Rosenzweig, N. Barov, and E. Colby, IEEE Trans. Plas. Sci. **24**, 409 (1996).
[15]S. G. Anderson and J. B. Rosenzweig, Phys. Rev. ST Accel. Beams **3**, 094201 (2000).
[16]J. B. Rosenzweig, A. M. Cook, R. J. England, M. Dunning, S. G. Anderson, and M. Ferrario, Nucl. Instr. Meth. A **557**, 87 (2006).
[17]Y. Li, S. Chemerisov, and J. Lewellen, Phys. Rev. ST Accel. Beams **12**, 020702 (2009).
[18]M. Berz, *Modern Map Methods in Particle Beam Physics* (Academic Press, London, 1999).
[19]H. Zhang and M. Berz, Nucl. Instrum. Meth. A **645**, 338 (2011).
[20]A. Valfells, D. W. Feldman, M. Virgo, P. G. O'Shea, and Y. Y. Lau, Phys. Plasmas **9**, 2377 (2002).
[21]K. L. Jensen, P. G. O'Shea, D. W. Feldman, and J. L. Shaw, J. Appl. Phys. **107**, 014903 (2010).
[22]P. Musumeci, J. T. Moody, R. J. England, J. B. Rosenzweig, and T. Tran, Phys. Rev. Lett. **100**, 244801 (2008).
[23]O. J. Luiten, S. B. van der Geer, M. J. de Loos, F. B. Kiewiet, and M. J. van der Wiel, Phys. Rev. Lett. **93**, 094802 (2004).
[24]R. Akre, D. Dowell, P. Emma, J. Frisch, S. Gilevich, G. Hays, Ph. Hering, R. Iverson, C. Limborg-Deprey, H. Loos *et al.*, Phys. Rev. ST Accel. Beams **11**, 030703 (2008).